The Discovery of the Largest Gas Filament in Our Galaxy, or a New Spiral Arm?

Chong Li[1,2] , Keping Qiu[1,2] , Bo Hu[1,2] , and Yue Cao[1,2]

[1] School of Astronomy and Space Science, Nanjing University, 163 Xianlin Avenue, Nanjing 210023, People's Republic of China; kpqiu@nju.edu.cn
[2] Key Laboratory of Modern Astronomy and Astrophysics (Nanjing University), Ministry of Education, Nanjing 210023, People's Republic of China

Abstract

Using the Five-hundred-meter Aperture Spherical radio Telescope (FAST), we detect a giant H I filamentary structure in the sky region of $307°\!.7 < \alpha < 311°\!.0$ and $40°\!.9 < \delta < 43°\!.4$. The structure has a velocity range of -170 to -130 km s^{-1}, and a mean velocity of -150 km s^{-1}, putting it at a Galactocentric distance of 22 kpc. The H I structure, which we name Cattail, has a length of 1.1 kpc, which so far appears to be the furthest and largest giant filament in the Galaxy. Its mass is calculated to be $6.5 \times 10^4\ M_\odot$ and the linear mass density is 60 $M_\odot$ pc^{-1}. Its width is 207 pc, corresponding to an aspect ratio of 5:1. Cattail possesses a small velocity gradient (0.02 km s^{-1} pc^{-1}) along its major axis. Together with the HI4PI data, we find that Cattail could be even longer, up to 5 kpc. We also identify another new elongated structure as the extension into the Galactic first quadrant of the Outer Scutum–Centaurus (OSC) arm, and Cattail appears to be located far behind the OSC arm. The question about how such a huge filament is produced at this extreme Galactic location remains open. Alternatively, Cattail might be part of a new arm beyond the OSC arm, though it is puzzling that the structure does not fully follow the warp of the Galactic disk.

Unified Astronomy Thesaurus concepts: Interstellar filaments (842); Interstellar atomic gas (833)

1. Introduction

It has been realized that filaments are one of the basic structures in the interstellar medium (Myers 2009; André et al. 2014). With high spatial resolutions and sensitivities in the submillimeter regime, Herschel observations reveal the ubiquitous presence of filaments in the dense parts of molecular clouds, which are also most closely related to star formation (André et al. 2010; Men'shchikov et al. 2010; Schneider et al. 2012, 2013; Gong et al. 2018; Zhang et al. 2019). The largest elongated molecular cloud structures are called giant (molecular) filaments with lengths greater than 10 pc. Jackson et al. (2010) have identified an archetypal giant filament "Nessie" with an extreme aspect ratio (80×0.5 pc) and claimed that the dense cores within it are the birthplaces of massive stars. Goodman et al. (2014) claimed that Nessie has a much larger length of 430 pc and referred it as the "bone" of the Scutum–Centaurus arm. After Nessie, a large number of observational studies aimed at identifying and characterizing giant filaments have been performed in various tracers, ranging from extinction maps at mid-infrared (Ragan et al. 2014; Zucker et al. 2015) to far-infrared/submillimeter dust emission (Wang et al. 2015; Abreu-Vicente et al. 2016) and CO line emissions (Su et al. 2015; Xiong et al. 2017; Li et al. 2018a, 2020).

Zucker et al. (2018) have performed a comprehensive analysis of the physical properties of large-scale filaments in the literature. Possibly related to the mechanisms shaping the structure and dynamics of the Milky Way (Smith et al. 2014a), together with the spatial resolution and sensitivity limitations of the observations, no giant filament is found in the Extreme Outer Galaxy (EOG) where the Galactocentric distance ($R_{\rm gc}$) is greater than 15 kpc. 85% of giant filaments lie mostly parallel to $<45°$, and in close proximity to <30 pc, the Galactic plane. There are 30%–45% of giant filaments that are associated with spiral arms. The lengths of the giant filaments range from 11–269 pc and the furthest filament is located at $R_{\rm gc} \sim 12$ kpc, well within the most remote spiral arms ($R_{\rm gc} \sim 20$ kpc; Dame & Thaddeus 2011;

Sun et al. 2015; Reid et al. 2016) and the furthest molecular clouds ($R_{\rm gc} \sim 30$ kpc; Digel et al. 1994; Matsuo et al. 2017).

Compared to giant molecular filaments, H I filaments are not well studied. Kalberla et al. (2016) and Soler et al. (2020) systematically searched for H I filaments in the Galaxy using the large-scale H I surveys Galactic All-Sky Survey (GASS; McClure-Griffiths et al. 2009) and the HI/OH Recombination line survey of the inner Milky Way (THOR; Beuther et al. 2016; Wang et al. 2020), respectively. Most of the H I filaments are aligned with the Galactic plane, which is similar to the situation of giant molecular filaments. Combined with the Planck all-sky map of the linearly polarized dust emission at 353 GHz, Kalberla et al. (2016) found that H I filaments tend to be associated with dust ridges and aligned with magnetic fields. They claimed that the cold neutral medium is mostly organized in sheets and that they are observed as filaments due to projection effects. The H I filaments are normally cold with a typical excitation temperature $T_{\rm ex} \sim 50$ K and are often associated with CO dark molecular gas (Kalberla et al. 2020). However, detailed physical properties of H I filaments, as well as their distribution in the Galaxy, are not well characterized. A specific case is presented in Soler et al. (2020): using the $40''$ resolution observations in the THOR survey, they identified a very long H I filament "Magdalena" in the inner Galaxy ($R_{\rm gc} \sim 12$ kpc) with a length exceeding 1 kpc (see Figure 9 in their paper).

In this work we present Five-hundred-meter Aperture Spherical radio Telescope (FAST) observations of a newly detected giant filamentary H I structure named Cattail, which is possibly the furthest ($R_{\rm gc} \sim 22$ kpc) and largest (~ 1.1 kpc) filament to date. Together with the archival HI4PI data, we find that Cattail could be even much longer (~ 5 kpc). A new extension of the Outer Scutum–Centaurus (OSC) arm between $70° < l < 100°$ is also identified. The observations are described in Section 2 and the results and discussion are presented in Section 3.
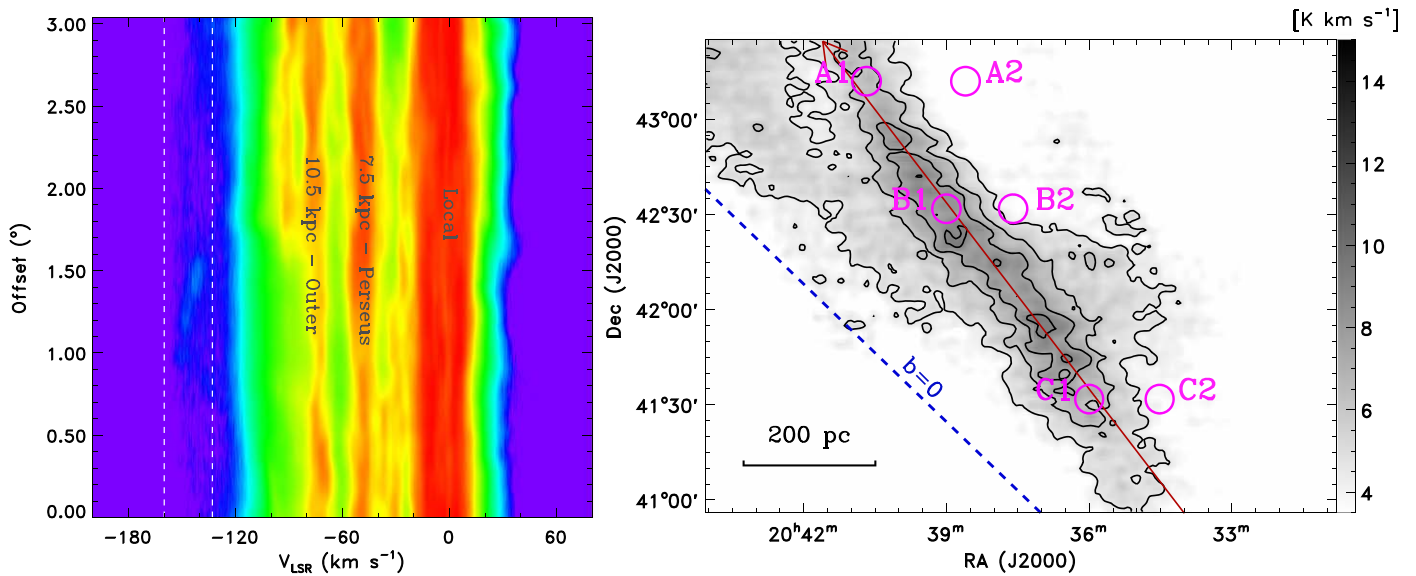
Figure 1. Left: Position–velocity map of the sky region along the red arrow marked in the right panel. The locations of the spiral arms are derived from Reid et al. (2014; 2016). The dashed lines indicate the approximate boundaries of the EOG feature. Right: Map of H I 21 cm emission intensity integrated from -160 to -140 km s^{-1}. The blue dashed line indicates the IAU-defined midplane. The purple circles indicate the positions of the spectra in Figure 2. The minimal level and interval of the overlaid contours are 4.5 and 1.5 K km s^{-1}, respectively.

2. Observation and Data Reduction

2.1. FAST Data

Using the FAST, the sky region of R.A. $307°\!\!.7 < \alpha < 311°\!\!.0$ and decl. $40°\!\!.9 < \delta < 43°\!\!.4$ was observed on 2019 August 24. The observations of the H I 1420.4058 MHz transition were carried out with the 19 beam L-band receiver (Li et al. 2018b). The ROACH back end contains 65,536 channels in the 32 MHz bandwidth, corresponding to a channel resolution of 0.476 kHz and a velocity resolution of 0.1 km s^{-1} at 1.420 GHz. The sky region was scanned along the R.A. in multibeam on-the-fly mode with a scanning rate of $15''$ s^{-1} and a dump time of 1 s. The rotating angle, which represents the cross angle between the 19 beam focal-plan array and line of decl., is set to be $23.4°$ for smooth super-Nyquist sampling.

During the observations, a 1.1 K noise from the diode was injected with a period of 2 s, which is synchronized with the sampling rate. Based on an absolute measurement of noise dipole and a factor derived by the difference between noise ON and OFF data for each beam, the observed data were calibrated into antenna temperature T_A in kelvin. Taking the beamwidth (FWHM) and aperture efficiency η from Jiang et al. (2020), we convert the antenna temperature (T_A) into brightness temperature (T_B). The aperture efficiency curves were obtained by repeating observations of the calibrator 3C286 at different zenith angles.

Using a Gaussian-smoothing kernel, the raw data are regridded and converted to a FITS data cube. The beamwidth is $3'$ and the pixel size of the FITS data cube is $1' \times 1'$. The typical system temperature during the observation is about 20 K and the rms sensitivity of our observation is estimated to be around 70 mK per channel. The pointing of the telescope has an rms accuracy of $7''\!\!.9$. We have compared the results of our data reduction with those of HI4PI (HI4PI Collaboration et al. 2016); the HI4PI and FAST H I emission profiles agree well with each other and the spectra LSR velocities are consistent.

2.2. HI4PI Data

This work makes use of data from an all-sky (4π sr) H I survey (HI4PI Collaboration et al. 2016). The HI4PI survey combines H I Northern Hemisphere data from the Effelsberg-Bonn HI Survey (EBHIS; Kerp et al. 2011; Winkel et al. 2016) obtained with the 100 m Effelsberg radio telescope with Southern Hemisphere data from GASS (McClure-Griffiths et al. 2009; Kalberla et al. 2010; Kalberla & Haud 2015) taken with the 64 m Parkes radio telescope. The angular and velocity resolutions of the final combined data are $16'\!\!.2$ and 1.29 km s^{-1}, respectively. The rms sensitivity of HI4PI H I data is about 43 mK. The LSR velocity coverage is about ± 600 km s^{-1} in the Northern Hemisphere and ± 480 km s^{-1} in the Southern Hemisphere.

3. Results and Discussion

The sky region of $20^{\mathrm{h}}30^{\mathrm{m}}48^{\mathrm{s}} <$ R.A. $< 20^{\mathrm{h}}44^{\mathrm{m}}04^{\mathrm{s}}$ and $40°\!\!.9 <$ decl. $< 43°\!\!.4$ covers the main part of the Cygnus-X North molecular cloud, which has a velocity range of -30 to 20 km s^{-1} (Schneider et al. 2010) and is located 1.4 kpc away from the Sun (Rygl et al. 2012; Xu et al. 2013). In Figure 1, however, there remains abundant atomic gas with velocities $<$ -30 km s^{-1}, implying the presence of H I gas far behind Cygnus-X. In the velocity range -170 to -130 km s^{-1}, there appears to be H I emission that is not connected to the main velocity components of the Outer arm. The central velocity of the outermost gas is -151.1 km s^{-1}. According to the rotation model of Reid et al. (2014; 2016), the heliocentric distance of such an H I cloud is ~ 21 kpc, corresponding to a distance from the Galactic center of ~ 22 kpc. The outermost cloud exhibits a filamentary structure and lies approximately parallel to the Galactic midplane ($b = 0$, right panel of Figure 1). Its length is about 1.1 kpc, much larger than the giant molecular filament Nessie, and comparable with the large H I filament Magdalena. If the structure, which we name Cattail, lies at the kinematic distance, it is located far beyond all known giant gas filaments ($R_{\mathrm{gc}} < 12$ kpc), molecular and atomic, in previous research
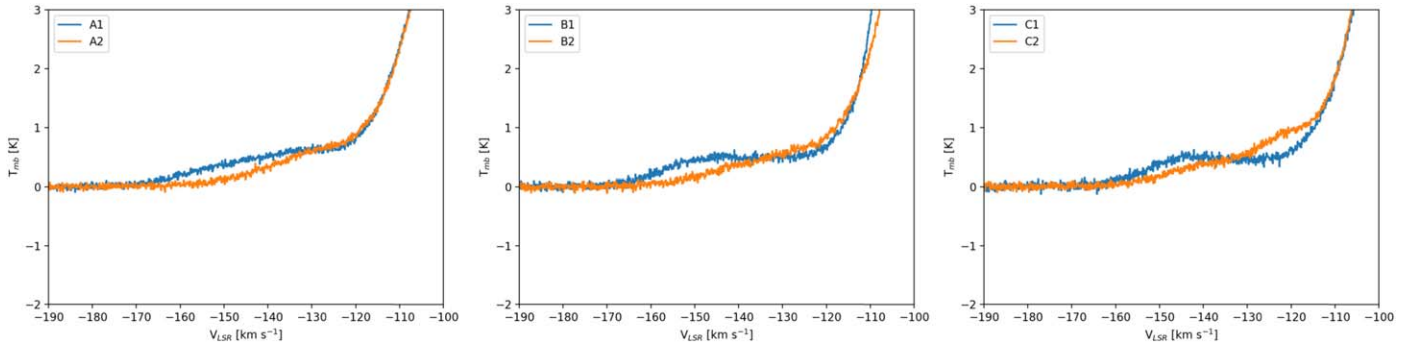
Figure 2. FAST H I spectra averaged over a $0°15 \times 0°15$ region taken from the six positions shown in Figure 1.
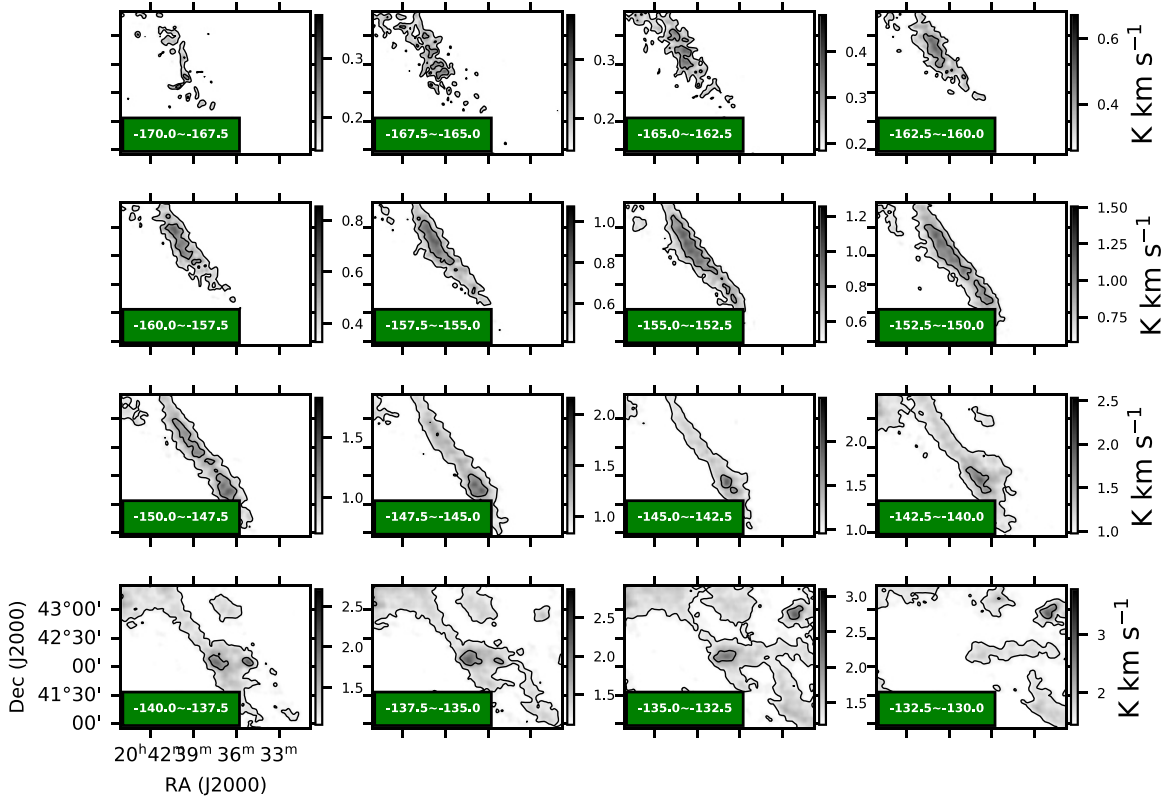

Figure 3. Velocity channel map of the H I 21 cm emission of Cattail. The minimal level of the contours is 0.55 times the emission peak and the interval is 0.25 times the peak.

(Zucker et al. 2018). Figure 2 presents the spectra of six positions located within (A1, B1, C1) and immediately outside of Cattail (A2, B2, C2). Compared to A2, B2, C2, the spectra of Cattail (A1, B1, C1) have an additional emission from -170 to -130 km s^{-1}. There is no self-absorption feature in the spectra.

Figure 3 shows the velocity channel map in the H I 21 cm emission of Cattail. It can be seen that the filament exhibits an overall velocity gradient along its major axis. The southwest end of Cattail has a less negative velocity compared to that of the northeast end. Most of the atomic gas of the filament has velocities in the range from -160 to -140 km s^{-1}, with a mean velocity of approximately -150 km s^{-1}. The intensity distribution and the width of the filament are almost uniform from northeast to southwest. The velocity gradient along the filament is estimated to be 0.02 km s^{-1} pc^{-1}.

Similar to Suri et al. (2019), we extract the radial profile of Cattail from the intensity map. First, we derive the direction of the filament spine, which is indicated by a red arrow in the right panel of Figure 1. Then, we extract the perpendicular intensity profile for each pixel along the filament spine. Finally, we average the profiles of all pixels along the filament and apply Gaussian fitting to the mean radial profile. In addition to the emission of Cattail, there is residual emission in the sky region which comes from the velocity distribution of the closer arms (Figure 2). In this case, the calculated width would increase with the fitting range (Smith et al. 2014b; Panopoulou et al. 2017). To be less influenced by this bias, we apply Gaussian fitting to the inner part of the radial profile. The intensity radial profile of Cattail is almost symmetrical (Figure 4). The width (FWHM) of the filament is 207 pc, which means that the aspect ratio of Cattail is about 5:1. Given that the width is comparable
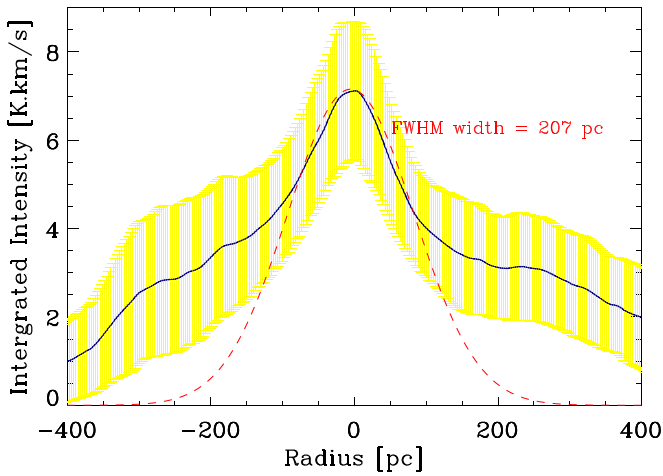
Figure 4. Mean radial intensity profile perpendicular to Cattail. The position of the peak intensity is regarded as the center of the profile, i.e., the position of $R = 0$. The negative and positive distances correspond to the southeast and northwest sides of the filament. The yellow area shows the $\pm 1\sigma$ dispersion of the radial profile distribution. The dashed red curve shows the Gaussian fitting to the inner part of the profile.

Table 1
Physical Parameters of Cattail

Parameter	Value
Galactic longitude l	$81°49$
Galactic latitude b	$0°65$
R.A. αJ2000	$20^h37^m54^s$
Decl. δJ2000	$+42^d14^m40^s$
Center velocity	-151.1 km s^{-1}
Kinematic distance D	21 kpc
Galactocentric radius R_{gc}	22 kpc
Length	1.1 kpc
Width (FWHM)	207 pc
Aspect ratio	5:1
Mass	$6.5 \times 10^4 \, M_\odot$
Linear mass	$60 \, M_\odot$ pc^{-1}
Line width ΔV	12 km s^{-1}
Peak column density	1.7×10^{19} cm^{-2} ($0.1 \, M_\odot$ pc^{-2})
Peak volume density	0.03 cm^{-3}

Note. Rows 1–5 give the central positions in the position–position–velocity (PPV) space. The kinematic distance is derived according to the Galactic rotation model A5 of Reid et al. (2014). The volume density is defined as $N_{H\,I}$/depth, where depth is assumed to be the same as width.

to the scale height of gas in a spiral arm (Kalberla & Kerp 2009), Cattail could also be a density enhancement along a spiral arm; we will come back to this point later.

Considering that the peak antenna temperature is about 1 K (Figure 2) and there is no H I narrow self-absorption feature in the spectra (see Figure 2), the emission should be optically thin and the column density can be calculated according to the following formula (Wilson et al. 2009):

$$N_{H\,I} \, [\text{cm}^{-2}] = 1.823 \times 10^{18} \int T_B(v) dv \, [\text{K km s}^{-1}] \qquad (1)$$

We calculated the mass of Cattail to be $6.5 \times 10^4 \, M_\odot$. The linear mass density is $60 \, M_\odot$ pc^{-1}. The peak column density of Cattail is 1.7×10^{19} cm^{-2} ($0.1 \, M_\odot$ pc^{-2}), which is close to the median value of H I filaments with latitudes $|b| > 20°$ (Kalberla et al. 2016) and lower than the threshold ($N \geqslant 1 \times 10^{22}$ cm^{-2}) for high-column-density gas adopted by Zucker et al. (2018). Assuming the depth to be the same as the width (207 pc), the peak volume density of the filament is calculated to be 0.03 cm^{-3}, which is close to the average Galactic midplane volume density at $R_{gc} = 22$ kpc (0.01 cm^{-3}) (Kalberla & Kerp 2009). The physical parameters of Cattail are listed in Table 1.

Both simulations (Inutsuka & Miyama 1992, 1997) and observations (André et al. 2010; Men'shchikov et al. 2010; Schneider et al. 2012, 2013) have shown that filaments tend to be vulnerable to radial collapse if the line mass is greater than the critical value defined as $M_{vir} = 2\sigma_{tot}^2/G$ (Fiege & Pudritz 2000). The total velocity dispersion σ_{tot} can be obtained by the FWHM line width ($\Delta v/\sqrt{8 \ln 2}$), which is 12 km s^{-1} for Cattail. H I filaments are normally cold with a typical excitation temperature $T_{ex} \sim 50$ K (Kalberla et al. 2020), corresponding to an isothermal sound speed of approximately 0.65 km s^{-1}. Therefore, the turbulence may be supersonic in Cattail. The critical line mass M_{vir} is calculated to be $1.1 \times 10^4 \, M_\odot$ pc^{-1}, which is much larger than the linear mass density M_{line} (60 $M_\odot$ pc^{-1}). Thus, Cattail is gravitationally unbound and may be in an expanding state, unless confined by an external pressure (Fischera & Martin 2012).

A velocity range of $|V_{LSR}| > 90$ km s^{-1} is generally used to separate high-velocity clouds (HVCs) from gas at low and

intermediate velocities. However, this operational definition is insufficient considering that the velocities of some clouds can be well understood in terms of Galactic rotation but exceed 90 km s^{-1} (Reid et al. 2016). Similarly with Wakker (1991), we adopt a "forbidden velocity" of $|V_{LSR} - V_{rot}| > 50$ km s^{-1} to identify HVCs, where V_{rot} is the rotation curve of the Milky Way. In the direction of Cattail, the filament can be an HVC only when its heliocentric distance is within 12.5 kpc ($R_{gc} <$ 14 kpc). However, the Galactic latitude of Cattail is $0°65$, which would put it within the flaring FWHM of the disk when $R_{gc} < 14$ kpc (Kalberla & Kerp 2009). As HVCs travel through hot halo gas, they would be heated and photon ionized, which causes thermal instabilities between the skin and the inner region of the clouds (Putman et al. 2012). Moreover, the headwind pressures can induce dynamical instabilities, e.g., shear-driven disturbance in HVCs, which makes them fragment into head-tail clouds (Butler Burton et al. 2004) and increase their line widths (Putman et al. 2011). The H I 21 cm line width of Cattail is 12 km s^{-1}, significantly smaller than the typical value of 20–30 km s^{-1} for HVCs (Lockman 2003; Tumlinson et al. 2017; Barger et al. 2020). The cloud does not seem to be fragmenting. Also, Cattail has a filamentary morphology parallel to the Galactic midplane with a mass less than $10^5 \, M_\odot$, and if it is an HVC, it would have been fully ionized while passing through the Galaxy halo (Bland-Hawthorn et al. 2007; Heitsch & Putman 2009; Kwak et al. 2011). Therefore, the properties of Cattail do not appear to be compatible with those of an HVC.

Assuming that the velocity of Cattail is attributed to the Galactic rotation, the structure is located beyond all the known spiral arms in the first quadrant. We then examine other possible origins of the extreme velocity of Cattail. We have discussed above that Cattail does not seem to be an HVC. Combining the results of Anderson et al. (2014) and Green (2014), there are no supernova remnants or H II regions with regular sizes $>2°5$ near Cattail. There is no dwarf satellite galaxy near Cattail either (McConnachie 2012). Hence, there is no evidence for Cattail's velocity coming from the influences of stellar feedback or a tidal stream, and the most likely explanation is the Galactic rotation. Moreover, taking the
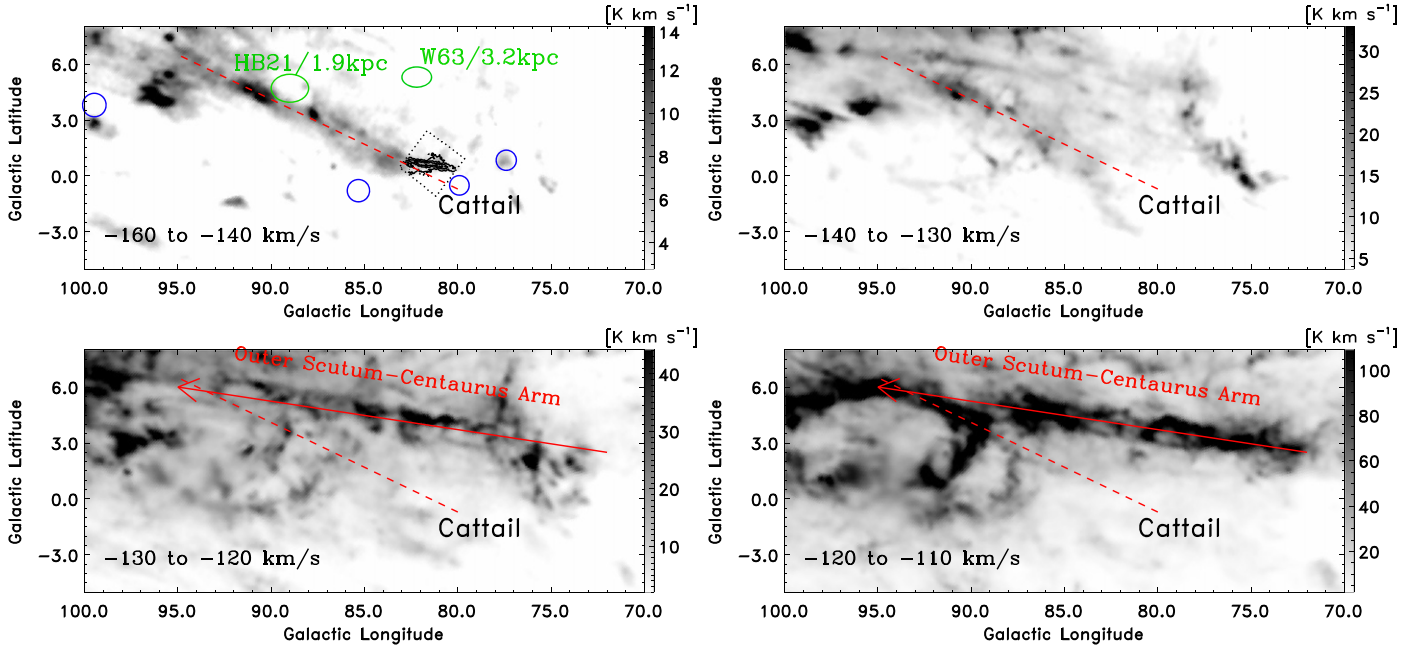
Figure 5. H I integrated intensity maps of the HI4PI data in the velocity ranges from -160 to -140 km s^{-1}, -140 to -130 km s^{-1}, -130 to -120 km s^{-1} and -120 to -110 km s^{-1}, respectively. The dashed box in the top-left panel indicates the survey region of FAST observation. The green and blue ellipses indicate the locations of the Galactic supernova remnants and H II regions with angular sizes $>1°$. The red arrows indicate the path of the position–velocity plot in Figure 6.

column density and the depth of Cattail to be 1.7×10^{19} cm^{-2} and $\sim 0°\!.5$, respectively, the volume density of Cattail would be significantly lower than the typical value of the Milky Way when it is located at $R_{gc} < 15$ kpc (Kalberla & Kerp 2009). Both a filament and a spiral arm should have a large density contrast compared to the surrounding medium. Therefore, we consider that Cattail is located at a heliocentric distance and Galactocentric distance of ~ 20 kpc.

Using the HI4PI data, we have investigated the complete morphology of Cattail (Figure 5). Cattail exhibits an even larger dimension while retaining a coherent velocity of -160 to -140 km s^{-1}. The FAST observations cover the southwest end of the full structure while the northeast end is located at about $l = 93°$ and $b = 5°\!.5$. We designate them as the FAST end and HI4PI end in this work, respectively. The full length of the complete Cattail reaches $\sim 15°$ (5 kpc).

In the velocity range from -130 to -110 km s^{-1}, there is another new elongated structure between $70° < l < 100°$. From its morphology (Figure 5) and velocity (Figure 6), it is apparently the extension of the OSC arm previously only seen at $0° < l < 70°$ (Dame & Thaddeus 2011). The full structure of the OSC arm in the first Galactic quadrant is then seen for the first time. In projection, Cattail is connected to the OSC arm at about $l = 93°$. However, Cattail does not appear to be physically connected to the OSC arm. First, the velocity of Cattail is different from that of the OSC arm by 30 km s^{-1}. Second, if Cattail is connected to the OSC arm at a Galactic longitude of about $93°$ and extends to about $80°$, it means that Cattail joins the OSC arm at the downstream end with respect to the Galactic rotation and leaves the arm toward the upstream end, i.e., in a pattern opposite to the inertial direction of the Galactic rotation; such a structure is inconsistent with the picture of a spur originating from a spiral arm (e.g., Dobbs & Bonnell 2006). Thus, when combining the large-scale map of HI4PI, Cattail may have a much larger dimension but still appears to be located well above the OSC arm.
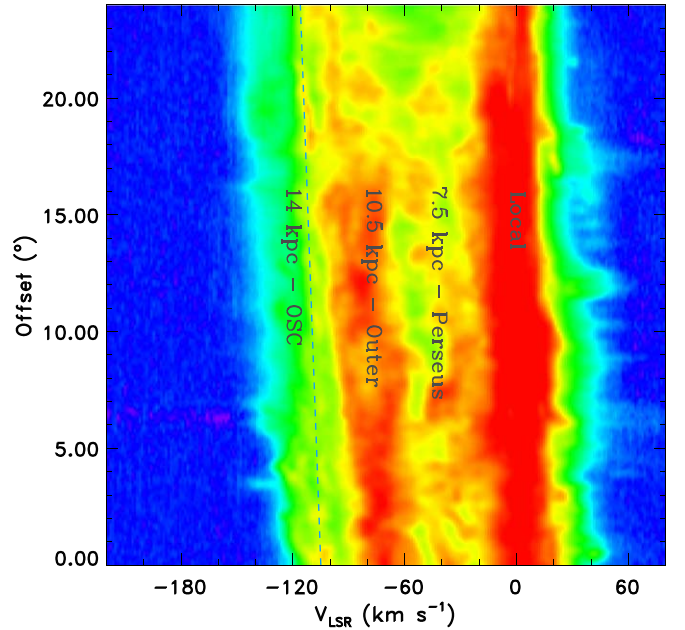

Figure 6. Position–velocity map along the arrow marked in Figure 5.

Based on the above analysis, we suggest two possible explanations for Cattail: it is a giant filament with a length of ~ 5 kpc, or part of a new arm in the EOG (Figure 7). Until recently, simulations of giant filaments appeared in the literature. As the numerical simulations show, the shear from Galactic rotation plays a critical role in the formation of large-scale filaments (Smith et al. 2014a; Duarte-Cabral & Dobbs 2016). Since the shearing motion tends to stretch out and align gas with spiral arms, giant filaments tend to form in spiral arms and interarm regions. Unlike most of the giant molecular filaments that are associated with spiral arms and lie
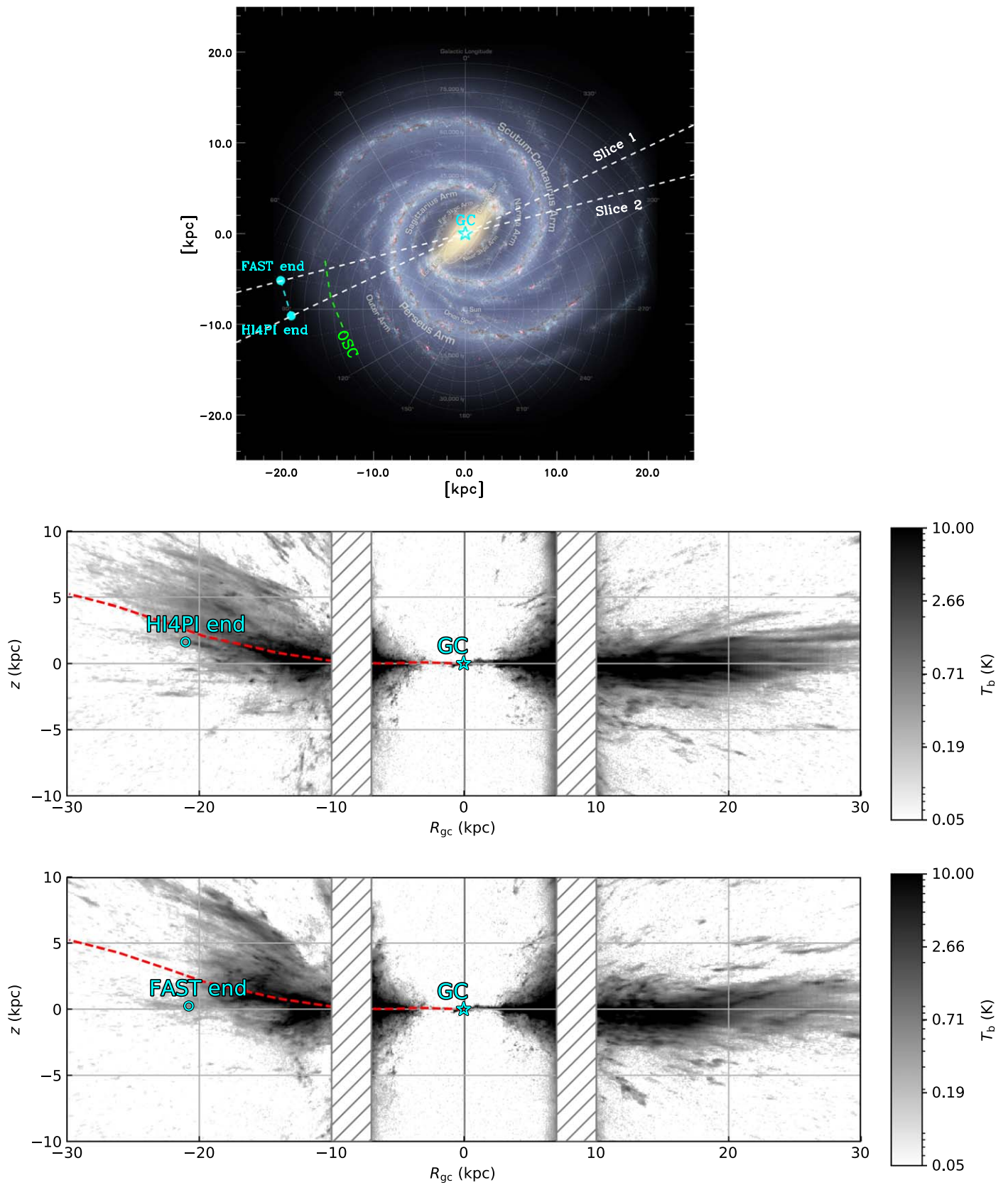
5

Figure 7. Top: Artist's conception of the Milky Way (R. Hurt: NASA/JPL-Caltech/SSC). The new part of the OSC and the Cattail identified in this work are indicated with the green and blue dashed lines, respectively. Middle: Intensity distribution along slice 1 in the top panel, which derived from the HI4PI data under the Galactic rotation model A5 of Reid et al. (2014). The red dashed line indicates a sketch of the warped plane near Cattail derived from Levine et al. (2006) and Kalberla & Kerp (2009). Bottom: intensity distribution along slice 2 in the top panel.

within 30 pc from the physical Galactic midplane (Wang et al. 2016; Zucker et al. 2018), Cattail is far beyond the outermost OSC arm. Figure 7 shows that the Galactic disk is significantly warped in the first quadrant of the EOG, which is in line with the forecasts from Levine et al. (2006), Kalberla et al. (2007), and Kalberla & Kerp (2009). The Z-scale height of the HI4PI end is about 2 kpc, which approximates the warped scale of the physical Galactic midplane at that Galactocentric distance. Comparatively, the FAST end of Cattail is located at a Galactic latitude of $0°.65$, corresponding to about 200 pc upon the IAU-defined midplane ($b = 0°$), which is flat from the Galactic center to the edge of the Galaxy. Thus, the complete Cattail may originate from the warped physical Galactic midplane at a longitude of $\sim93°$ and extend to a longitude of $\sim80°$ with $Z \sim 200$ pc. If Cattail is a gas filament located beyond the OSC arm, how is such a huge structure formed? Alternatively, if Cattail is part of a new spiral arm in the EOG, it is also puzzling that the new arm does not fully follow the Galactic warp, given that the FAST end is about 1.8 kpc away from the warped Galactic disk midplane. While these questions remain open with the existing data, the observations provide new insights into our understanding of the Galactic structure.

ORCID iDs

Chong Li ⓘ https://orcid.org/0000-0003-2218-3437
Keping Qiu ⓘ https://orcid.org/0000-0002-5093-5088
Bo Hu ⓘ https://orcid.org/0000-0002-3286-5469
Yue Cao ⓘ https://orcid.org/0000-0002-6368-7570

References

Abreu-Vicente, J., Ragan, S., Kainulainen, J., et al. 2016, A&A, 590, A131
Anderson, L. D., Bania, T. M., Balser, D. S., et al. 2014, ApJS, 212, 1
André, P., Di Francesco, J., Ward-Thompson, D., et al. 2014, in Protostars and Planets VI, ed. R. S. Klessen et al. (Tucson, AZ: Univ. Arionza Press), 27
André, P., Men'shchikov, A., Bontemps, S., et al. 2010, A&A, 518, L102
Barger, K. A., Nidever, D. L., Huey-You, C., et al. 2020, ApJ, 902, 154
Beuther, H., Bihr, S., Rugel, M., et al. 2016, A&A, 595, A32
Bland-Hawthorn, J., Sutherland, R., Agertz, O., & Moore, B. 2007, ApJL, 670, L109
Butler Burton, W., Braun, R., & de Heij, V. 2004, in High Velocity Clouds, ed. H. van Woerden et al. (Dordrecht: Kluwer), 313
Dame, T. M., & Thaddeus, P. 2011, ApJL, 734, L24
Digel, S., de Geus, E., & Thaddeus, P. 1994, ApJ, 422, 92
Dobbs, C. L., & Bonnell, I. A. 2006, MNRAS, 367, 873
Duarte-Cabral, A., & Dobbs, C. L. 2016, MNRAS, 458, 3667
Fiege, J. D., & Pudritz, R. E. 2000, MNRAS, 311, 85
Fischera, J., & Martin, P. G. 2012, A&A, 542, A77
Gong, Y., Li, G. X., Mao, R. Q., et al. 2018, A&A, 620, A62
Goodman, A. A., Alves, J., Beaumont, C. N., et al. 2014, ApJ, 797, 53
Green, D. A. 2014, BASI, 42, 47
Heitsch, F., & Putman, M. E. 2009, ApJ, 698, 1485
HI4PI Collaboration, Ben Bekhti, N., Flöer, L., et al. 2016, A&A, 594, A116
Inutsuka, S.-I., & Miyama, S. M. 1992, ApJ, 388, 392
Inutsuka, S.-i., & Miyama, S. M. 1997, ApJ, 480, 681
Jackson, J. M., Finn, S. C., Chambers, E. T., Rathborne, J. M., & Simon, R. 2010, ApJL, 719, L185
Jiang, P., Tang, N.-Y., Hou, L.-G., et al. 2020, RAA, 20, 064
Kalberla, P. M. W., Dedes, L., Kerp, J., & Haud, U. 2007, A&A, 469, 511
Kalberla, P. M. W., & Haud, U. 2015, A&A, 578, A78
Kalberla, P. M. W., & Kerp, J. 2009, ARA&A, 47, 27
Kalberla, P. M. W., Kerp, J., Haud, U., et al. 2016, ApJ, 821, 117
Kalberla, P. M. W., Kerp, J., & Haud, U. 2020, A&A, 639, A26
Kalberla, P. M. W., McClure-Griffiths, N. M., Pisano, D. J., et al. 2010, A&A, 521, A17
Kerp, J., Winkel, B., Ben Bekhti, N., Flöer, L., & Kalberla, P. M. W. 2011, AN, 332, 637
Kwak, K., Henley, D. B., & Shelton, R. L. 2011, ApJ, 739, 30
Levine, E. S., Blitz, L., & Heiles, C. 2006, ApJ, 643, 881
Li, C., Wang, H., Zhang, M., et al. 2018a, ApJS, 238, 10
Li, C., Wang, H., Zhang, M., Ma, Y., & Lin, L. 2020, ApJS, 249, 27
Li, D., Wang, P., Qian, L., et al. 2018b, IMMag, 19, 112
Lockman, F. J. 2003, ApJL, 591, L33
Matsuo, M., Nakanishi, H., Minamidani, T., et al. 2017, PASJ, 69, L3
McClure-Griffiths, N. M., Pisano, D. J., Calabretta, M. R., et al. 2009, ApJS, 181, 398
McConnachie, A. W. 2012, AJ, 144, 4
Men'shchikov, A., André, P., Didelon, P., et al. 2010, A&A, 518, L103
Myers, P. C. 2009, ApJ, 700, 1609
Panopoulou, G. V., Psaradaki, I., Skalidis, R., Tassis, K., & Andrews, J. J. 2017, MNRAS, 466, 2529
Putman, M. E., Peek, J. E. G., & Joung, M. R. 2012, ARA&A, 50, 491
Putman, M. E., Saul, D. R., & Mets, E. 2011, MNRAS, 418, 1575
Ragan, S. E., Henning, T., Tackenberg, J., et al. 2014, A&A, 568, A73
Reid, M. J., Dame, T. M., Menten, K. M., & Brunthaler, A. 2016, ApJ, 823, 77
Reid, M. J., Menten, K. M., Brunthaler, A., et al. 2014, ApJ, 783, 130
Rygl, K. L. J., Brunthaler, A., Sanna, A., et al. 2012, A&A, 539, A79
Schneider, N., Csengeri, T., Bontemps, S., et al. 2010, A&A, 520, A49
Schneider, N., Csengeri, T., Hennemann, M., et al. 2012, A&A, 540, L11
Schneider, N., Csengeri, T., Hennemann, M., et al. 2013, A&A, 551, C1
Smith, R. J., Glover, S. C. O., Clark, P. C., Klessen, R. S., & Springel, V. 2014a, MNRAS, 441, 1628
Smith, R. J., Glover, S. C. O., & Klessen, R. S. 2014b, MNRAS, 445, 2900
Soler, J. D., Beuther, H., Syed, J., et al. 2020, A&A, 642, A163
Su, Y., Zhang, S., Shao, X., & Yang, J. 2015, ApJ, 811, 134
Sun, Y., Xu, Y., Yang, J., et al. 2015, ApJL, 798, L27
Suri, S., Sánchez-Monge, Á, Schilke, P., et al. 2019, A&A, 623, A142
Tumlinson, J., Peeples, M. S., & Werk, J. K. 2017, ARA&A, 55, 389
Wakker, B. P. 1991, A&A, 250, 499
Wang, K., Testi, L., Burkert, A., et al. 2016, ApJS, 226, 9
Wang, K., Testi, L., Ginsburg, A., et al. 2015, MNRAS, 450, 4043
Wang, Y., Beuther, H., Rugel, M. R., et al. 2020, A&A, 634, A83
Wilson, T. L., Rohlfs, K., & Hüttemeister, S. 2009, Tools of Radio Astronomy (Berlin: Springer)
Winkel, B., Kerp, J., Flöer, L., et al. 2016, A&A, 585, A41
Xiong, F., Chen, X., Yang, J., et al. 2017, ApJ, 838, 49
Xu, Y., Li, J. J., Reid, M. J., et al. 2013, ApJ, 769, 15
Zhang, M., Kainulainen, J., Mattern, M., Fang, M., & Henning, T. 2019, A&A, 622, A52
Zucker, C., Battersby, C., & Goodman, A. 2015, ApJ, 815, 23
Zucker, C., Battersby, C., & Goodman, A. 2018, ApJ, 864, 153